S S C C ELSEVIER

Contents lists available at ScienceDirect

Experimental Thermal and Fluid Science

journal homepage: www.elsevier.com/locate/etfs





Unsteady boundary-layer transition measurements with Temperature-Sensitive Paint under cryogenic conditions[☆]

Armin Weiss ^{a, *}, Christian Klein ^a, Ulrich Henne ^a, Anne Hebler ^{b, 1}

- ^a Institute of Aerodynamics and Flow Technology, German Aerospace Center (DLR), Bunsenstraße 10, 37073 Göttingen, Germany
- ^b Institute of Aeroelasticity, German Aerospace Center (DLR), Bunsenstraße 10, 37073 Göttingen, Germany

ARTICLE INFO

Keywords: Boundary-layer transition Unsteady aerodynamics Pitch oscillation Temperature-Sensitive Paint (TSP) Large Reynolds number Heat-transfer coefficient

ABSTRACT

The study presents the first measurement of boundary-layer transition on a harmonically-pitching airfoil under cryogenic conditions. The experiments were conducted in the cryogenic wind tunnel of the German-Dutch Wind Tunnels in Cologne using a test rig especially designed for harmonic pitch oscillations of a twodimensional model equipped with the laminar NLF(2)-0415 airfoil. The tests were performed at free stream Reynolds and Mach numbers of $Re = 6 \times 10^6$ and M = 0.34. Unsteady pitch oscillations were investigated at different pitch frequencies (up to 40 Hz, i.e. a reduced frequency of 0.540) and pitch amplitudes, as well as for a steady angle-of-attack polar for comparison. The boundary-layer transition movement was captured by means of spatially high-resolving temperature-sensitive paint using a surface-integrated heating layer of carbon nanotubes (cntTSP) and fast-response pressure transducers. The cntTSP data was processed according to the already established "Differential Thermography" (DT) method as well as using a recently presented method based on the evaluation of the qualitative distribution of the heat-transfer coefficient (HTC). The techniques are described in detail and results are evaluated with respect to measurement-based thermal hysteresis as well as the influence of varying pitch frequency and amplitude. The latter could successfully be measured by all applied methods. The findings further reveal significant improvements in the detection of unsteady boundarylayer transition when applying the HTC method compared to DT. These are: a reduction of the measurement error in terms of the thermal hysteresis component in the results and an increased result density at pitch phases, where the DT method inherently fails to yield results.

1. Introduction

According to the International Air Transport Association IATA [1] the ${\rm CO_2}$ emissions during the lifecycle of commercial aircraft need to be reduced drastically by 2050 in order to achieve the stated "net-zero" requirements. A promising aerodynamic remedy to reduce the fuel consumption and polluting emissions is Natural Laminar Flow (NLF) technology for the wings of future commercial aircraft. The technology reduces the overall friction drag on the wing surfaces by exploiting the limits of laminar boundary-layer flow which produces less wall shear stress than turbulent boundary-layers.

Recently, the NLF concept was applied to an innovative transport aircraft configuration with forward-swept wings by Seitz et al. [2]. It is the declared goal of the research initiative ECOWING (Wing

Technology Validation for Ultra Green Aircraft, 2020–2021)² and its successor ULTIMATE (Ultra High Efficient Wing and Movables for Next Generation Aircraft, 2022–2026)³ to demonstrate the capabilities of this aircraft configuration numerically and experimentally under realistic flight conditions, i.e. at large Reynolds- and Mach numbers. Previous studies on different laminar airfoils showed that the operational flight envelope is significantly affected in terms of flutter stability when allowing free laminar boundary-layer flow as compared to configurations where the boundary-layer was tripped to be entirely turbulent [3,4]. In order to assess the risks associated with flutter instability due to unforced boundary-layer transition, it is essential to capture the movement of boundary-layer transition during pitch-oscillation.

Sensor-based methods for the detection of boundary-layer transition on oscillating airfoils use hot-film sensors [5] or pressure transducers when employing the so-called σc_p method according to Gardner and

 $^{^{}m th}$ This work was conducted in the framework of the DLR research project ULTIMATE.

^{*} Correspondence to: Institute of Propulsion Technology, German Aerospace Center (DLR), Linder Höhe, 51147 Cologne, Germany. E-mail address: armin.weiss@dlr.de (A. Weiss).

¹ Institute of Test and Simulation for Gas Turbines, German Aerospace Center (DLR), Forschungsallee 1, 86159 Augsburg, Germany.

 $^{^{2}\,}$ As part of the German economic stimulus programme KoPa 33.

³ As part of the sixth German aeronautical research programme LuFo VI-2.

Nomenclature			
$\overline{\alpha}$	Mean angle-of-attack, deg		
\hat{lpha}	Pitch amplitude, deg		
c	Chord length, $c = 0.400 \mathrm{m}$		
c_{s}	Specific heat capacity of the model surface,		
	J/(kg K)		
$E_{ m nr}$	Activation energy for non-radiative process,		
	J/mol		
f	Pitch frequency, Hz		
h	Heat transfer coefficient, $W/(m^2 K)$		
Ι	Luminescent intensity or image gray level, counts		
\Re	Universal gas constant, J/(mol K)		
k	Reduced pitch frequency, $k = \pi f c/U_{\infty}$		
$\lambda_{ m s}$	Thermal conductivity normal to model surface, W/(K m)		
M	Mach number		
$q_{ m CNT}$	Heat flux applied through CNT, W/m ²		
q_h	Convective heat flux, W/m ²		
$ ho_{ m s}$	Model surface density, kg/m ³		
Re	Chord Reynolds number		
s_T	Temperature sensitivity, $s_T = \frac{1}{I} \frac{\partial I}{\partial T}$, K ⁻¹		
t	Time, s		
tf	Relative phase of pitch cycle		
$\Delta t f$	Relative phase difference between pro-		
<i>T</i>	cessed images		
T	TSP-surface temperature, K		
T_{∞}	Free stream flow temperature, K		
U_{∞} CNT	Wind tunnel flow velocity, m/s Carbon nanotubes		
DT			
DIT	Differential infrared thermography		
DLR	Differential infrared thermography German Aerospace Center		
DNW	German Dutch wind tunnels		
HTC	Heat transfer coefficient		
IATA	International Air Transport Association		
NLF	Natural laminar flow		
PU	Poly urethane		
IR	Infrared		
TSP	Temperature-sensitive paint		
$\sigma c_{ m p}$	Standard deviation of pressure signal		
Hoff	CNT heating was turned off		
Hon	CNT heating was turned on 2s prior to		
	image acquisition		
ref	Reference conditions		

Richter [6]. Hot-film sensors measure local changes of the heat transfer at the sensor, which is directly coupled to changes of the local wall shear stress through the Reynolds-Colburn analogy [7,8] and hence indicative of boundary-layer transition from laminar to turbulent. In turn, the σc_p method exploits the fact that boundary-layer transition causes an unsteady "kink" in the pressure distribution [9]. In the case of pitch-oscillating airfoils, the position of the kink varies from one pitch-cycle to the next. Therefore, the cycle-to-cycle standard-deviation of a pressure signal (σc_p) comprises a relative maximum at those phases during the pitch cycle when boundary-layer transition moves across the specific pressure tap location on the surface. However, the spatial resolution of all discrete sensor-based methods is inherently limited by their distribution on the model surface.

The limited spatial resolution has been significantly increased by non-intrusive thermal imaging methods using infrared cameras (IR) or temperature-sensitive paint (TSP). The TSP technique is based on the photokinetic interaction between the airflow and a luminescent coating on the surface of interest. A comprehensive description and review of the method is provided by Liu et al. [10]. When excited by light of a certain wavelength, the quantum efficiency of the ensuing luminescence decreases with increasing temperature due to non-radiative relaxation processes of the excited molecule. The relation between the luminescent intensity I and the absolute temperature T can be described by the Arrhenius equation

$$\ln \frac{I(T)}{I(T_{\rm ref})} = \frac{E_{\rm nr}}{\Re} \left(\frac{1}{T} - \frac{1}{T_{\rm ref}} \right), \tag{1}$$

where $E_{\rm nr}$ is the activation energy for the non-radiative process, \Re is the universal gas constant and $T_{\rm ref}$ is a reference temperature in Kelvin.

Thermal methods use the different heat transfer characteristics between laminar and turbulent boundary layers to give an indication of the boundary-layer transition location. An artificially produced temperature difference between the wind tunnel flow and the model surface is usually applied because it increases the surface temperature difference between laminar and turbulent boundary layers compared with the natural difference based on the respective recovery temperatures [11]. This artificially induced temperature difference is commonly applied, for instance, by modification of the free stream temperature, known as "T-step method" [12]. Alternatively, the model surface can be actively heated using external lamps or even a surface-integrated heating layer. Klein et al. [13] developed the cntTSP method, where a spray-coated and electrically contacted heating layer consisting of carbon nanotubes (cnt) is directly integrated into the layer setup of a TSP coating. cntTSP was shown to enable successful measurement of boundary-layer transition on a steady airfoil under cryogenic conditions [14]. For steady airfoil aerodynamics, thermal methods identified the maximum temperature gradient on a heated or cooled airfoil surface as corresponding to the transition position (see e.g. [15]). However, this methodology is known to be less useful when applied to pitch-oscillating airfoils; this is because within a pitch cycle, the local temperature differences due to the moving transition position are small when compared to the cycle-averaged surface temperature differences [16,17].

This problem was solved by "Differential Infrared Thermography" (DIT), which was developed in the context of unsteady helicopter aerodynamics in order to probe the movement of boundary-layer transition during pitch-oscillation. A comprehensive analysis and review of the method is detailed in the work of Wolf [18]. For DIT, two thermal images of e.g. a heated model surface are acquired in direct succession with a short time delay. The temperature difference between those images can be attributed to the moving transition position and hence evaluated to detect the intermediate transition location. The measurement principle was demonstrated by Raffel and Merz [19] and validated against results from hot-film sensors and pressure transducers by Richter et al. [20]. The method was further numerically analyzed by Gardner et al. [16] and experimentally optimized by Wolf et al. [17]. Since the basic methodology can be equivalently used for analyzing TSP images, the term "Differential Thermography" (DT) is used in this work.

The DT approach was successfully applied to TSP intensity data of an airfoil during quasi-steady pitch-sweep by Yorita et al. [21]. Ikami et al. [22] introduced a new method to detect boundary-layer transition data on pitch-oscillating airfoils. They employed TSP in order to process a phase-resolved surface distribution of the heat transfer coefficient (HTC) and identified its maximum gradient as corresponding to the transition location. They applied the technique as a proof of principle on a harmonically pitching airfoil under atmospheric and low Reynolds number conditions at comparatively low frequencies of up to $4.2\,\mathrm{Hz}$, which corresponded to a reduced frequency of k=0.10.

This paper presents the capabilities of TSP to measure unsteady boundary-layer transition on a harmonically pitching airfoil for the first



Fig. 1. Downstream view (in direction of wind tunnel flow) of the cntTSP-coated wind tunnel model in the test section.

time under cryogenic conditions. In addition to previous works, the results obtained from thermal DT and HTC methodologies are compared to each other and to the established sensor-based σc_n method. The findings are then evaluated in terms of erroneous measurementinduced thermal hysteresis and effects with respect to pitch frequency and amplitude.

2. Experimental techniques

2.1. Test setup and instrumentation

The wind tunnel tests were conducted in the cryogenic wind tunnel in Cologne of the German-Dutch Wind Tunnels (DNW). The Göttingentype wind tunnel had a $2.4\,\mathrm{m} \times 2.4\,\mathrm{m}$ test section and a custom designed pitch oscillation setup [3] for cryogenic tests on unsteady 2D-airfoil models. The test rig comprised a hydraulic actuator to enforce harmonic pitch oscillations of the investigated 2D model of a modified natural laminar flow airfoil (NLF(2)-0415, see [3] and also Fig. 4). The model was installed vertically and clamped between turntables in the wind tunnel test section, as pictured in Fig. 1. The sinusoidal movement of the model is characterized by the mean angle-of-attack $\overline{\alpha}$, the pitch amplitude $\hat{\alpha}$ and the pitch frequency f, as illustrated in Fig. 2. The wind tunnel flow was set to $U_{\infty} = 93 \,\mathrm{m/s}$ and cooled down to $T_{\infty} = 179 \,\mathrm{K}$, yielding flow Mach and Reynolds numbers (based on chord length) of M = 0.34 and Re = 6×10^6 . All reported test conditions are summed up in Table 1. This includes the pitch settings for a steady airfoil polar, a study with varying pitch frequency and two sets of conditions where the pitch amplitude was varied at constant settings for mean angle-of-attack and pitch frequency (noted as pitch amplitude study in Table 1).

A sketch of the instrumented wind tunnel model is provided in Fig. 3. The model was made out of carbon-fiber reinforced plastic (CFRP), spanning across the entire 2.4 m height of the test section

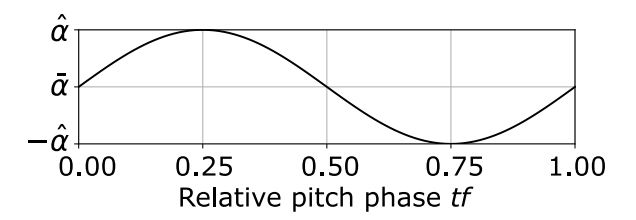


Fig. 2. Sinusoidal movement of pitch angle α around mean angle-of-attack $\overline{\alpha}$ with pitch amplitude $\hat{\alpha}$ and pitch frequency f for an entire pitch cycle.

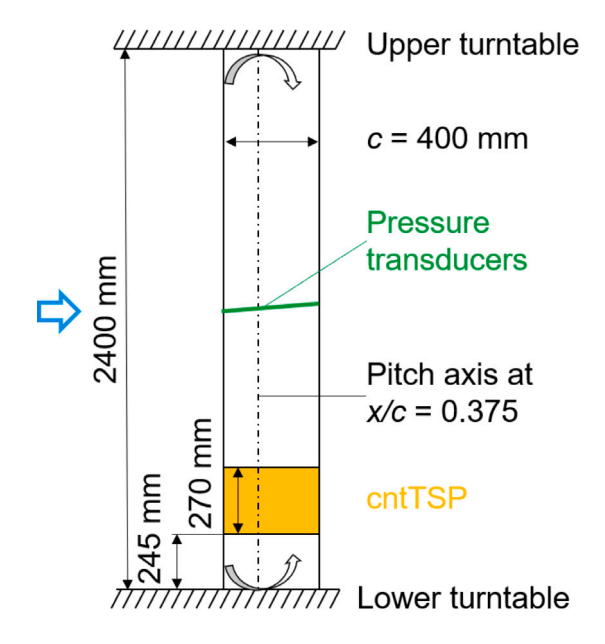


Fig. 3. Schematic sketch of wind tunnel model with indicated dimensions and installed instrumentation.

Source: Modified from [3].

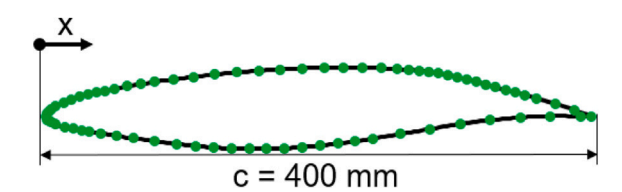


Fig. 4. Modified NLR(2)-0415 airfoil [3] and positions of 75 installed fast-response pressure transducers.

and comprising a chord length of $c = 400 \,\mathrm{mm}$. It was instrumented with 75 fast-response pressure transducers of differential type (Kulite CCQ-132X-093-5D), see Fig. 4 for their positioning.

The cntTSP coating was placed on the lower side of the model for reasons of better optical access to the airfoil suction side. The distance between the cntTSP coated area and the lower turntable was 245 mm which is greater than the peniche thickness of 90 mm for halfmodel testing in this wind tunnel and therefore beyond the wind tunnel boundary-layer [23]. The heated TSP area covered 270 mm of the span, the entire 400 mm of the suction side of the model and 75% of the pressure side. The cntTSP setup used for this study was described in detail by Klein et al. [24] so only the essentials are summarized in the following. A sketch of the applied coating layers is provided in Fig. 5. The model surface was first coated with a primer layer. A first polyurethane (PU) based white screen layer was then used between the primer and the carbon nanotube layer to ensure electrical insulation with respect to the model and to provide thermal insulation of the model surface. A second PU screen layer was used in between the

Table 1
Test conditions.

Flow conditions	$M = 0.34$; Re = 6×10^6 ; $U_{\infty} = 93 \text{ m/s}$; $T_{\infty} = 179 \text{ K}$; $c = 0.4 \text{ m}$		
Study	ā, °	â, °	$k \left(= \pi f c / U_{\infty} \right)$
Steady airfoil	0-1.0 (Δ = 0.2); 1.1;1.2-2.0 (Δ = 0.2)	_	-
Pitch frequency	1.2	0.2	0.108; 0.270; 0.540
Pitch amplitude	1.2	0.1; 0.2; 0.4; 0.6; 0.8; 1.0	0.108
	1.6	0.2; 0.4; 0.6	0.108

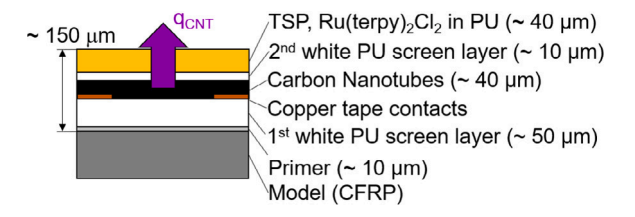


Fig. 5. Layer setup of cntTSP coating, see Klein et al. [24] for details.

carbon nanotubes and the TSP to reflect and hence enhance the emitted TSP luminescence. On this second screen layer, black dot markers were applied for image alignment during post processing. For the evaluated wind tunnel runs, the carbon nanotube coating was powered using 360 V and 0.54 A yielding an electrical heat flux of $q_{\rm CNT}\approx 1\,{\rm kW/m^2}$ to the surface. It should be mentioned that the heat fraction lost due to conduction into the model was not quantified. However, the insulating (PU) screen layer between the model surface and the CNT was chosen five times thicker than the screen layer between the CNT and TSP layers such that the assumption is justified that the largest heat portion is directed towards the TSP layer on top of the surface. As detailed in Section 3.2.2, the amount of electrical heat flux does not need to be known exactly, since only the qualitative distribution of the heat flux coefficient is used to determine the transition location.

The final TSP layer comprised ${\rm Ru(terpy)_2Cl_2}$ as temperature-sensitive luminophore embedded into a PU matrix. After coating, the final layer was polished to yield an average roughness of ${\it Ra} \ll 0.2~\mu{\rm m}$ which is essential for boundary-layer transition tests under high Reynolds number conditions. The TSP sensor has been characterized by Klein et al. [25] as having a temperature sensitivity of $s_T = -0.036~{\rm K}^{-1}$ at 180 K, where the TSP temperature sensitivity is defined as the relative intensity change per unit Kelvin.

$$s_T = \frac{1}{I} \frac{\partial I}{\partial T} \tag{2}$$

The TSP was excited by two LEDs (*Hardsoft Illuminator*) with peak emission wavelengths of 462 nm. The luminescence signal was captured by a *Photron FASTCAM Mini AX200* camera using a band-pass filter $(605 \pm 27.5 \text{ nm})$ to separate the usable signal from the excitation light. This setup yielded a spatial image resolution of approximately 770 pixel/chordlength, viz. 1.9 pixel/mm.

2.2. Data acquisition and pre-processing

2.2.1. Pressure data and angle-of-attack

The sampling rate of angle-of-attack and surface pressure recordings was linked to the pitch frequency of the model such that 128 samples were recorded during one pitch cycle, i.e. $f_{acq.}=128\cdot f$. For pitch frequencies between f=4–40 Hz, this resulted in recordings of 160–640 pitch cycles. Before the signal was processed to find transition locations, as explained in Section 3.2.3, the mean value was subtracted and the signal was band-pass filtered between 2 Hz and the Nyquist theorem frequency corresponding to the respective sampling rate of the test point.

2.2.2. TSP data

For steady pitch cases, 1000 images were recorded at 250 fps during two subsequent phases. First, reference ("ref") images were acquired under the conditions listed in Table 1. Secondly, so-called "run"-images were acquired using the "temperature-step" (T-step) procedure [15], while the free-stream temperature was lowered by a few Kelvin through an increase of the liquid nitrogen mass flow into the test section.

For unsteady test conditions, images were acquired under "heat-off" conditions while the CNT heating was turned off (denoted using the subscript $_{Hoff}$ further below) as well as under "heat-on" conditions (denoted as $_{Hon}$). Note that for the "heat-on" condition, the CNT heating was turned on 2 s prior to acquisition of the first image. For each acquisition phase approximately 4000 images were acquired at a frame rate of 1 kHz, which was phase locked to the pitch frequency. This yielded between 250 images per cycle at $f=4\,\mathrm{Hz}$ and 25 images per cycle at $f=40\,\mathrm{Hz}$. The correspondingly sampled phase resolutions were $\Delta t f=0.004$ and $\Delta t f=0.04$ at $f=4\,\mathrm{Hz}$ and 40 Hz.

For the unsteady measurement points, a random relative movement between camera and model was noticed, this being likely attributable to vibrations caused by the pitch oscillation module. Therefore, all images were aligned with the first image of each sequence before they could be further processed. For this purpose, fifteen black dot markers had been applied to the TSP coating, see Section 2.1. The following steps were then carried out using the inhouse developed software package ToPas as in [26]

- · Marker Registration
- · Image alignment using a second order polynomial warp function
- · Cycle averaging of all images
- Image division and algebraic operations according to the algorithms described in Sections 3.2.1 and 3.2.2

All further processing steps, including the assignment of pitch phase and angle-of-attack, and the application of the transition detection algorithms (see Sections 3.2.1, 3.2.2 and 3.2.3) were performed using Python. This includes also the span-wise averaging of image data across a region covering $150 \, \mathrm{px}$, i.e. $78 \, \mathrm{mm}$ span. This area had been selected in order to avoid the influence of turbulent wedges which were identified during post processing (see e.g. Fig. 8 close to $y = 55 \, \mathrm{mm}$).

3. Boundary-layer transition detection

This section presents the transition detection methods used in this paper. A detailed evaluation of the techniques and comparison between the respective results is presented in Section 4.

3.1. Steady conditions

On the steady model, boundary-layer transition was measured using the established T-step method [12]. The results had already been presented by Klein et al. [24], who showed that they are interchangeable with results deduced using the CNT heating method but superior in signal-to-noise ratio. For the T-step method, the adiabatic surface temperature difference between laminar and turbulent areas is increased by temporarily increasing the injection rate of liquid nitrogen into the wind tunnel free stream, which acts as a negative temperature step of the flow with respect to the model surface. The transition positions were then derived at the point corresponding to the maximum gradient

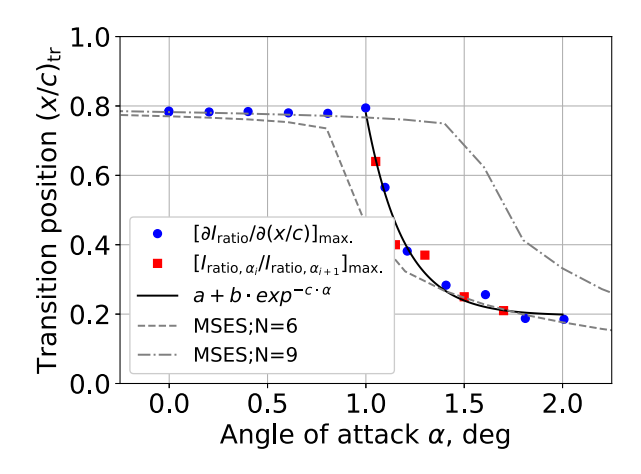


Fig. 6. Transition results of steady airfoil obtained from experimental data (T-step, DT and exponential fit) and 2D coupled Euler-/boundary-layer computations with critical N-factors of N=6 and N=9. Exponential fit constants are a=0.1956; b=104.7531 and c=5.1907.

of the TSP intensity ratio between images acquired at different free stream temperatures [27]. The results are presented using blue dots (•) in Fig. 6, where transition location versus angle-of-attack have been plotted. Since the differential thermography (DT) technique outlined in Section 3.2.1 is based on a spatial change of the transition location and the resulting change of surface temperature, it can also be applied to thermal images of a steady angle-of-attack polar. This had been done previously by Wolf et al. [17], who evaluated surface temperature differences of test points corresponding to succeeding angles-of-attack. Accordingly, the resulting location where the temperature difference peaks marks the transition position of the intermediate angle-of-attack. The procedure eventually increases the sampling of transition locations at angles-of-attack which were not approached during data acquisition. The corresponding results are included in Fig. 6 using red squares (.). Note, that the temperature differences for these results were evaluated in a qualitative manner only by dividing images corresponding to succeeding angles-of-attack α_i and α_{i+1} (see Eq. (3)).

The results in Fig. 6 show that transition from laminar to turbulent flow does not occur further downstream than at $(x/c)_{\rm tr}=0.8$. For $\alpha>1$ deg transition moves gradually upstream up to $(x/c)_{\rm tr}=0.2$ at $\alpha=2.0$ deg. For comparisons with unsteady transition locations (see Fig. 17), the steady experimental results were approximated using a non-linear least-squares fit to the exponential function $(x/c)_{\rm tr}=a+b\cdot exp^{-c\cdot\alpha}$. The constant values are indicated in the caption of Fig. 6.

For comparison with experimental results, computations were performed using the coupled 2D Euler-/ boundary-layer code MSES [28, 29] for the investigated airfoil with transition N-factors of N=6 and N=9. These results are also shown in Fig. 6. Note that the experimental results are within the bounds spanned by the numeric calculations. Moreover, the MSES computations yield a similar upstream movement of the transition location at increasing angle-of-attack as the experimental data as well as the same downstream limit of transition to turbulence at $(x/c)_{tr}=0.8$.

3.2. Unsteady conditions

3.2.1. Differential thermography (DT)

The following section concentrates on the fundamentals of the technique and its application when using TSP. The principles were originally derived for the so-called "DIT" technique (using IR cameras). As they apply for the use of TSP as well, the term "Differential Thermography" (DT) is used here.

Richter et al. [20] and Gardner et al. [16] showed that the peak location of the model surface temperature difference between two

angles-of-attack, α_i and α_{i+1} , at succeeding phase positions, tf_i and tf_{i+1} , corresponds to the point of 50% turbulence intermittency at the intermediate angle-of-attack $(\alpha_i + \alpha_{i+1})/2$. This peak location is further referred to as "transition position". For TSP, a first order Taylor series expansion of the Arrhenius relation in Eq. (1) approximates the intensity ratio of subsequently acquired images at different angles-of-attack as a function of the corresponding temperature difference:

$$\frac{I(T_{\alpha_{i}})}{I(T_{\alpha_{i+1}})} = 1 - \frac{E_{nr}}{\Re \cdot T_{\alpha_{i+1}}^2} \left[T_{\alpha_{i}} - T_{\alpha_{i+1}} \right]. \tag{3}$$

Note that the intensity ratio yields values less than one for positive temperature differences, i.e. $T_{\alpha_i} > T_{\alpha_{i+1}}$, and vice versa negative differences. Assuming changes to be small, the use of the linear relationship between intensity ratio and temperature difference given in Eq. (4) is justifiable:

$$T_{\alpha_{i}} - T_{\alpha_{i+1}} = \frac{2}{s_{T}} \left[\frac{\frac{I(T_{\alpha_{i}})}{I(T_{\alpha_{i+1}})} - 1}{\frac{I(T_{\alpha_{i}})}{I(T_{\alpha_{i+1}})} + 1} \right]$$
(4)

The temperature sensitivity is assumed to be constant at s_T $-0.036\,\mathrm{K^{-1}}$. The value corresponds to the temperature sensitivity at $T = 180 \,\mathrm{K}$, which was investigated by Klein et al. [25] for the same TSP sensor as used in this study (see Fig. 1 in [25]). The DT principle is sketched schematically in Fig. 7 for a heated model surface. During the upstroke pitching motion with $\alpha_i < \alpha_{i+1}$, boundary-layer transition moves upstream and yields $T_{a_{\rm i}} > T_{a_{\rm i+1}}$ in the transition zone due to the larger, more efficiently cooled area at α_{i+1} (see top of Fig. 7). The opposite holds during the downstroke. Thus, for TSP data the transition position is found by searching for the minimum and maximum peak locations of the intensity ratio or, as illustrated in the lower graph of Fig. 7, the maximum and minimum temperature differences during upstroke and downstroke, respectively. Moreover, Richter et al. [20] and Gardner et al. [16] showed experimentally and theoretically that due to thermal lag, the ΔT peak indicating boundary-layer transition according to the DT method is too far downstream during upstroke and too far upstream during downstroke when compared to the actual transition positions; these are also shown schematically in Fig. 7. In this context, the actual transition position corresponds to the location where 50% turbulence intermittency was detected using hot-film sensors [20]. A detailed discussion of thermal hysteresis and the associated results from this work are provided in Sections 3.2.4 and 4.1.

A sample TSP result during the upstroke pitching motion at k=0.108 is provided in Fig. 8. It displays the intensity ratio of two images acquired at a relative phase difference of $\Delta t f=0.080$ and corresponds to an instantaneous angle-of-attack of $\alpha=1.8$ deg at 5.6% of the pitch cycle $\alpha=1.6\pm0.6$ deg. The footprints of two turbulent wedges originating at the leading edge (and arising from transition occurring at this edge probably due to surface imperfections) are visible at $y=40\,\mathrm{mm}$ and $y=60\,\mathrm{mm}$. The transition area appears as a dark band in the span-wise region $70\,\mathrm{mm} < y < 250\,\mathrm{mm}$. The transition location is evaluated by detecting the minima or maxima across the span-wise averaged region between the two red lines which are indicated in Fig. 8.

The span-wise averaged intensity-ratio profile of the case displayed in Fig. 8 is plotted as temperature difference in Fig. 9 as gray and red lines. Note the small temperature differences of only $|\Delta T| < 0.1\,\mathrm{K}$ in the transition region. The red line shows the result after applying a moving average (width = $\Delta x/c = 0.025$) to the span-wise averaged data in gray. The corresponding temperature difference profile at the same instantaneous angle-of-attack but during downstroke ($\alpha = 1.8\,\deg \downarrow$) is displayed in blue and the profile corresponding to the maximum angle-of-attack during the same pitch cycle is added in black. The detected transition locations are marked by the correspondingly colored large dots. The results indicate that at $\alpha = 1.8\,\deg$ the transition location is further downstream during upstroke (red) as compared to during downstroke (blue). The transition movement therefore displays an expected hysteresis (see Section 3.2.4).

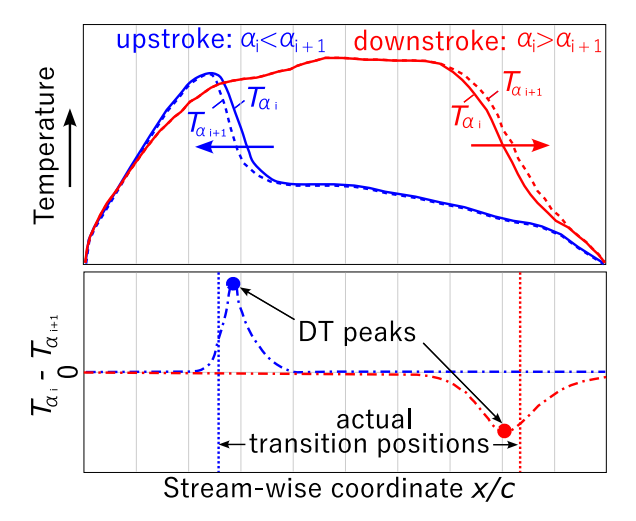


Fig. 7. Schematic of chord-wise temperature profiles of a heated model surface at consecutive pitch phases during up- and downstroke (top) and corresponding ΔT signals with identified transition positions according to the DT method and qualitative comparison to actual transition positions (bottom) as they can be identified using hot-film sensors.

Source: Figure modified from [17].

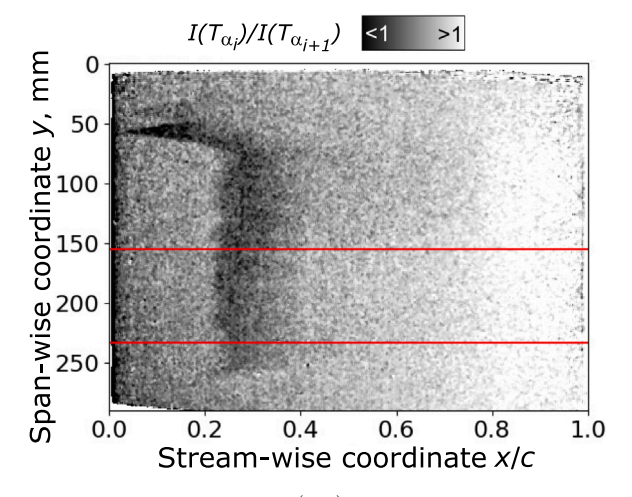


Fig. 8. Intensity ratio image $I(T_{a_i})/I(T_{a_{i+1}})$ corresponding to tf=0.056 and $\alpha=1.8$ deg during upstroke of pitch cycle with k=0.108; $\alpha=1.6\pm0.6$ deg.

A comparison between the displayed profiles in Fig. 9 reveals superimposed negative and positive gradients for the ΔT -profiles during upstroke and downstroke but no superimposed gradient for the profile corresponding to α_{max} . The α_{max} -profile results from a ratio of two images with the model at the same angle-of-attack, thus at the same relative position with respect to LED and camera. In contrast, during upstroke the trailing edge of the model moves away from LED and camera, which leads to larger luminescent intensities of trailing edge images at α_i as compared to α_{i+1} , where the trailing edge is slightly further away. Therefore, the resulting image ratio $I\left(T_{\alpha_i}\right)/I\left(T_{\alpha_{i+1}}\right)$ contains intensity differences which are independent of any temperature changes due to the moving boundary-layer transition on the model and which appear with opposite signs on the model with respect to its hinge point at x/c = 0.375 where no relative model movement occurred with respect to LED and camera. Hence, for the upstroke motion in Fig. 9, the values of $\Delta T > 0$ close to the leading edge and the values of $\Delta T < 0$ close to the trailing edge are artefacts due to the relative movement of the model with respect to light source and camera. The corresponding ΔT -profile during downstroke comprises the same artefacts but with opposite sign. These artefacts are known

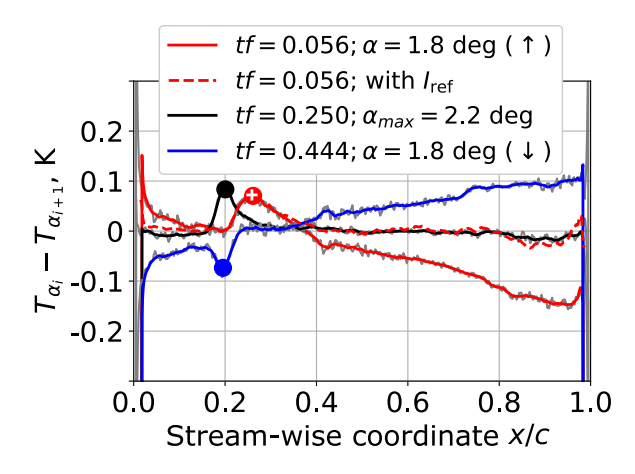


Fig. 9. Temperature difference signals at $k=0.108; \alpha=1.6\pm0.6$ deg and detected transition locations according to Eq. (4) (solid lines and circles) for different pitch phases. Results processed using additional *heat-off* reference image $I_{\rm ref}$ are added for tf=0.056 (dashed line and white cross). Colored lines show moving averages of spanwise averaged data in gray.

to the so-called TSP "intensity" method and can principally be avoided using the "lifetime" technique Yorita et al. [21]. In this work, the artefacts could be compensated by referencing the processed images, acquired under heat-on condition, to a reference image at the same phase position but acquired under heat-off condition before applying the ratio of consecutive images within the pitch cycle. A processed temperature profile during upstroke using such a reference image is displayed in Fig. 9 by the red dashed line. As expected, the superimposed negative gradient has disappeared and except for the transition region in vicinity of the positive ΔT -peak, the profile coincides with the profile at α_{max} comprising negligible temperature differences elsewhere. The corresponding detected transition position is marked by the white cross and coincides with the position detected without referencing which is marked by the red circular dot (•). As the demonstrated image referencing does not have an impact on the detected transition position, it was left out for further processing of other data points evaluated by the DT method. It should therefore be emphasized that the DT technique allows omitting reference images which are usually necessary when applying, for example, the T-step method for the detection of boundary-layer transition on steady airfoils.

The processed results are displayed in Fig. 10 for the entire pitch cycle showing the detected transition locations $(x/c)_{tr,DT}$ (lacktriangle) along with the corresponding angles-of-attack (•) against the relative pitch phase tf. The detected movement of boundary-layer transition follows the pitching motion. The transition location moves upstream during upstroke at increasing angles-of-attack and downstream during downstroke as the angle-of-attack decreases. The DT method relies on surface temperature changes between the time instances of the acquired images used to process the temperature change. As demonstrated by Wolf et al. [17], there are two main reasons for faulty or ambiguously detected transition locations using the DT method: First, at streamwise positions where the transition movement is fast with respect to small changes of the angle-of-attack. This occurs where the adverse pressure gradient on the airfoil is small and results in a smeared out ΔT signal comprising a double peak and leading to ambiguously detected transition positions. Secondly, close to and past the pitch reversal points, the ΔT -profiles comprise both minima from the downstroke movement and maxima from the upstroke movement. This is due to thermal hysteresis attributed to the model surface material, which has been analyzed in more detail by Gardner et al. [16]. Ambiguously detected ΔT -peaks were therefore manually removed from the results, see e.g. the "removed" data () as indicated in Fig. 10. In a last processing step for the DT method, the valid peaks were smoothed by a moving average corresponding to $\Delta t f = 0.08$, see e.g. the cyan-colored (*) "filtered" points in (Fig. 10).

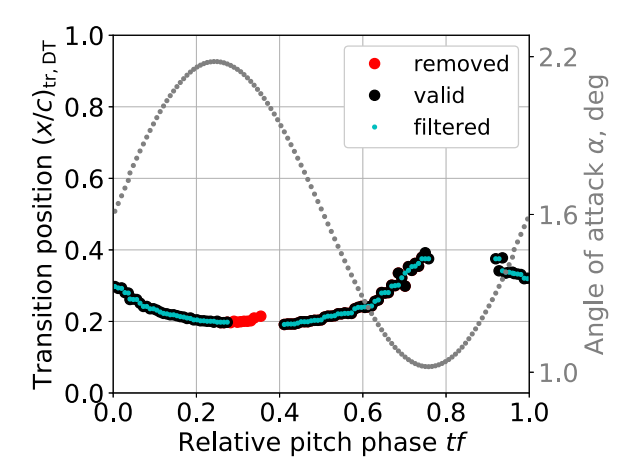


Fig. 10. Transition results using *Differential Thermography* at k = 0.108; $\alpha = 1.6 \pm 0.6$ deg.

3.2.2. Heat transfer coefficient (HTC)

It is known that boundary-layer transition is characterized by a sharp increase of the local skin friction coefficient [11]. Further, the local heat transfer coefficient between a model surface and fluid flow depends on the Prandtl number and follows the local shear stress, which was shown by the Reynolds-Colburn analogy [7,8]. In the presented work, the heat transfer coefficient h is determined qualitatively in order to derive its maximum positive gradient. This location is indicative for transition to turbulence of the laminar boundary-layer and therefore defined as transition location. The basics of the technique, which was first applied by Ikami et al. [22], are recaptured here in order to allow for a detailed comparison to other approaches used for the detection of boundary-layer transition on oscillating airfoils. Assuming an adiabatic model surface, i.e. neglecting conductive heat losses into the model as well as radiative heat losses, the resulting heat flux at the model surface $q(t_n)$ is the difference between the heat flux added by the carbonnanotube heating layer q_{CNT} and the convective heat flux of the flow

$$q(t_{\rm n}) = q_{\rm CNT} - q_h(t_{\rm n}) \tag{5}$$

Note that the following considerations pertain to the quantities at phase-averaged time instants $t_{\rm n}$ during the pitch cycle. $q_{\rm CNT}$ is calculated according to Eq. (6)

$$q_{CNT} = \frac{P_{el}}{A_{heated}} = 1 \frac{\text{kW}}{\text{m}^2},\tag{6}$$

considering the provided electrical power $P_{\rm el}$ and the heated surface across the coated area (see Fig. 3) on the model suction side and $\approx 75\%$ of the pressure side. The convective heat flux is expressed as a product of the heat transfer coefficient h and the temperature difference between the runs, when the heating had been switched on $\binom{1}{100}$ and off $\binom{1}{100}$:

$$q_h(t_n) = h \cdot \left[T_{\text{Hon}}(t_n) - T_{\text{Hoff}}(t_n) \right] \tag{7}$$

The temperature difference is evaluated in an analogous manner to Eq. (4). The surface heat flux can further be determined by the discretized formulation [30,31] of the relation between heat flux and temperature time-series [32,33].

$$q(t_n) = \frac{2\sqrt{\rho_s c_s \lambda_s}}{\sqrt{\pi}} \sum_{i=1}^{n} \frac{T(t_i) - T(t_{i-1})}{\sqrt{t_n - t_i} + \sqrt{t_n - t_{i-1}}}$$
(8)

 $\rho_{\rm s}, c_{\rm s}$ and $\lambda_{\rm s}$ are the model surface density, its specific heat capacity and thermal conductivity normal to the wall. The product in front of the summation in Eq. (8) (called the thermal parameter) serves as a scaling parameter of $q(t_{\rm n})$ and does not influence the qualitative distribution of h, which is obtained when solving Eq. (5) after substituting Eqs. (6)–(8). The thermal parameter was reasonably guessed to be $\left(\rho_{\rm s}c_{\rm s}\lambda_{\rm s}\right)_{\rm m}=0$

 $1.5 \times 10^6 \text{ J}^2/(\text{m}^4 \text{ K}^2 \text{ s})$, which lies in-between the values adopted by Gardner et al. [16] and Risius et al. [34], where the parameters had been estimated for a surface made from carbon-fiber reinforced plastic and calibrated for a different TSP coating as used in this study (without CNT). In Eq. (8), the temperature difference of subsequent time instants $T(t_i) - T(t_{i-1})$ practically corresponds to the term in Eq. (4), which is used for the evaluation according to the DT method. However, as discussed with respect to Fig. 9, the calculated temperature differences are biased by the model movement with respect to camera and light source when using phase-consecutive images of the heated run only. Therefore, the "heat-on" images are first normalized to the "heat-off" images at the same phase before the temperature difference between different phase positions is calculated. In this way, the temperature difference in Eq. (8) is calculated indirectly as described in Eq. (9). The relation assumes that the actual temperature changes seen in the T_{Hoff}-images are negligible throughout the pitch cycle and that the normalization step only corrects for the intensity change introduced by the model movement relative to light source and camera. Just as with the DT method, this post-processing step allows a free choice of the relative phase difference $\Delta t f$ between the respective image increments i and i-1, which are considered for calculation of the temperature differences in the summation of Eq. (8).

$$T(t_{i}) - T(t_{i-1}) = [T_{Hon}(t_{i}) - T_{Hoff}(t_{i})] - [T_{Hon}(t_{i-1}) - T_{Hoff}(t_{i-1})]$$

$$= \frac{2}{s_{T}} \begin{bmatrix} \frac{I(T_{a_{i},Hon})}{I(T_{a_{i},Hoff})} - 1\\ \frac{I(T_{a_{i},Hoff})}{I(T_{a_{i},Hoff})} + 1 \end{bmatrix} - \frac{2}{s_{T}} \begin{bmatrix} \frac{I(T_{a_{i-1},Hon})}{I(T_{a_{i-1},Hoff})} - 1\\ \frac{I(T_{a_{i-1},Hoff})}{I(T_{a_{i-1},Hoff})} + 1 \end{bmatrix}$$

$$(9)$$

According to the outlined HTC method the information of boundarylayer transition is contained in the sum of phase-averaged temperature differences from different phases in Eq. (8). To illustrate this concept, a temperature time series of the case presented in Figs. 8 and 9 was sampled at x/c = 0.22 and plotted across the pitch cycle, as shown in Fig. 11. The plot shows the local temperature at x/c = 0.22 with respect to the temperature sampled at the beginning of the pitch cycle at tf = 0. To ease interpretation, the relative pitch phase is also shown in the lower figure. Two distinct phase positions can be identified when the local temperature experiences sudden changes due to the change of the boundary-layer state at that position. As the angle-ofattack increases during upstroke at tf = 0.06 the surface temperature at x/c = 0.22 shows a sudden drop, which indicates the movement of the more efficiently cooling turbulent part of the boundary layer upstream x/c = 0.22. On the other hand, at tf = 0.47 during downstroke, the flow starts to re-laminarize at x/c = 0.22, leading to a relative temperature increase due to the less effective cooling of the laminar section of the boundary layer. Hence, in the period between 0.06 < tf < 0.47 the boundary-layer flow at x/c = 0.22 is turbulent and at other phases it is laminar, as indicated by the light red (turbulent) and dark red (laminar) stripes on top of Fig. 11.

The observed temporal change of the local model temperature was found to correlate with unsteady boundary-layer transition by Mertens et al. [35] who named the technique "Local Infrared Thermography" (LIT). They successfully validated the LIT technique by comparison to the σc_p and DT techniques.⁴ While both techniques, DT and LIT, analyze individual snapshots of the temporal change of the local surface

⁴ In their work, best agreement between LIT and DT results was found associating the relative pitch phase at the maximum local gradient $\partial T/\partial (tf)$ to boundary-layer transition. Further exploitation of the LIT method is not scope of this work.

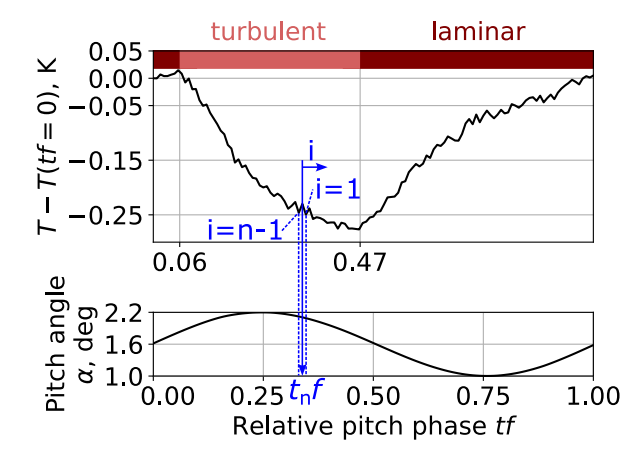


Fig. 11. Surface temperature change at x/c = 0.22 across the relative pitch phase with k = 0.108; $\alpha = 1.6 \pm 0.6$ deg (top) and pitch cycle (bottom).

temperature, the HTC method integrates the existing temporal temperature differences over the entire pitch cycle. In fact, and according to Eq. (8), the calculated heat flux at the time instant $t_{\rm n}$ includes a weighted sum of $f_{\rm acq}/f$ temperature differences. For instance, at a pitch frequency of f=8 Hz and an image acquisition rate of $f_{\rm acq}=1000\,{\rm Hz}$, which applies for the case presented in Fig. 11, there are 125 temperature differences considered for the heat flux result $q(t_{\rm n})$ at a distinct phase position. Note also, that the summation of a total of n temperature differences starts at the relative pitch phase of investigation $(t_{\rm n}f)$ with i=1 and the temperature difference of $T(t_1)-T(t_{\rm n})$. This ΔT signal is associated with the highest weighting factor (i.e. the denominator within the sum of Eq. (8)) of $1/\sqrt{\Delta t\,f}$ (since $\sqrt{t_{\rm n}-t_{\rm i-1}}=0$ for i=1).

A sample result image of the qualitative heat transfer coefficient h (see Eq. (7)) at tf=0.444 and during a pitch cycle with k=0.108 at $\alpha=1.6\pm0.6$ deg is presented in Fig. 12. The visible stream-wise contrast from bright to dark at $x/c\approx0.2$ clearly indicates boundary-layer transition from laminar to turbulent. Further downstream, the heat transfer coefficient decreases again, which is as expected due to the thickening of the boundary layer towards the trailing edge. Note also that the turbulent wedges at $y=40\,\mathrm{mm}$ and $y=60\,\mathrm{mm}$ also show increased values for the heat transfer coefficient; this had also been identified using the DT method in Fig. 8 for the same case. The transition locations derived from the HTC method were quantified using span-wise averages between the red lines in Fig. 12 which cover the same span-wise region as used for processing the DT data.

In Fig. 13, the span-wise averaged heat-transfer profiles are plotted against the stream-wise coordinate at the same phases and for the same case as presented for the DT evaluation method in Fig. 9. The span-wise averaged data (dashed curves) was smoothed by a spline fit (solid curves) before detecting the position of the maximum gradient $\partial h/\partial (x/c)|_{max}$ which corresponds to the transition location as reasoned above. The spline fitting was done using scipy's "UnivariateSpline" function in python 3.7 with a smoothing factor of 10⁵. The heat-transfer profiles in the figure allow a precise detection of the largest streamwise gradient which is indicated by the dots in Fig. 13. There is a dip with relatively low values for the heat transfer coefficient between 0.5 < x/c < 0.65. The dip is probably caused by in-homogeneities of both the surface heating $q_{\rm CNT}$ and of the model structure underneath the surface, which is hollow in that region and not supported by a sandwich core. Such in-homogeneities are not accounted for by the HTC algorithm, which expects homogeneous surface heating, i.e. a constant q_{CNT} , and neglects heat conduction into the model surface. However, the effect is significantly smaller than the more prominent change of the heat transfer coefficient due to boundary-layer transition.

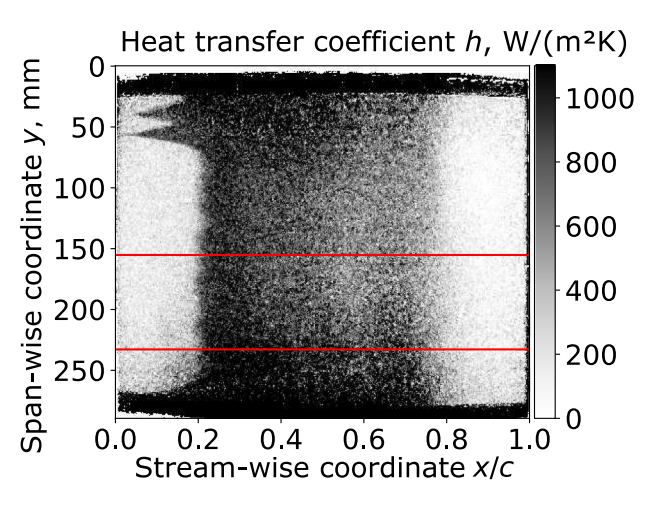


Fig. 12. Sample result of qualitative heat transfer coefficient h at tf = 0.444 during a pitch cycle with k = 0.108; $\alpha = 1.6 + 0.6$ deg.

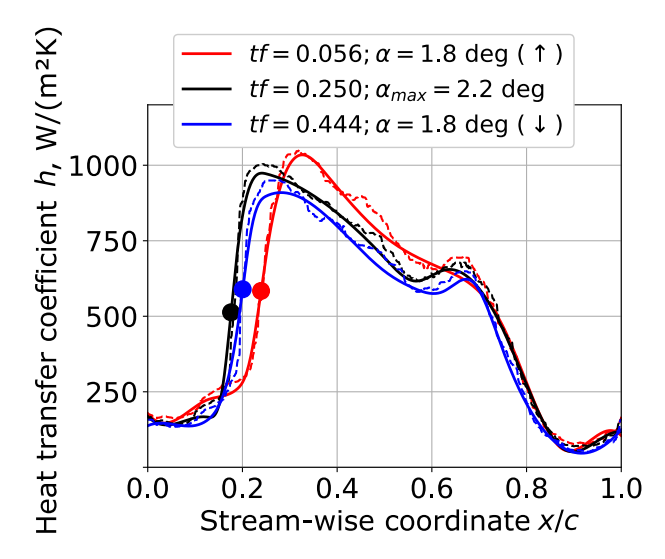


Fig. 13. Span-wise averaged heat transfer coefficient signals (dashed lines) at k = 0.108; $\alpha = 1.6 \pm 0.6$ deg and their corresponding smoothed curves (solid lines), with the detected transition locations (filled circles) based on the maximum gradient.

The boundary-layer transition movement detected by the HTC method is plotted for the entire pitch cycle in Fig. 14. The detected maxima of the heat-transfer profile (black dots) were smoothed by using a running median filter with $\Delta t f = 0.08$. In contrast to the DT method, the HTC algorithm detects plausible transition locations across the entire pitch cycle and even close to its reverse (turning) points. The graph indicates increased scatter of detected transition locations downstream of x/c > 0.5 where the transition position is sensitive to changes in pitch angle (see Fig. 6) and close to the down-stroke reversal point at $tf \approx 0.8$. The larger scatter in that region can partly be attributed to the in-homogeneous model structure in that region as mentioned above and partly also to the low signal-to-noise ratio of the ΔT values in areas where the transition position is particularly sensitive to a change in angle-of-attack and close to the pitch reversal points [17].

To conclude, the post-processing steps for the derivation of transition locations using the HTC method can be summarized as follows:

- 1. Alignment and cycle averaging of all recorded images
- 2. Image ratio calculation between "heat-on" and "heat-off" images for all pitch phases $I\left(T_{a_{\rm i},{\rm Hon}}\right)/I\left(T_{a_{\rm i},{\rm Hoff}}\right)$

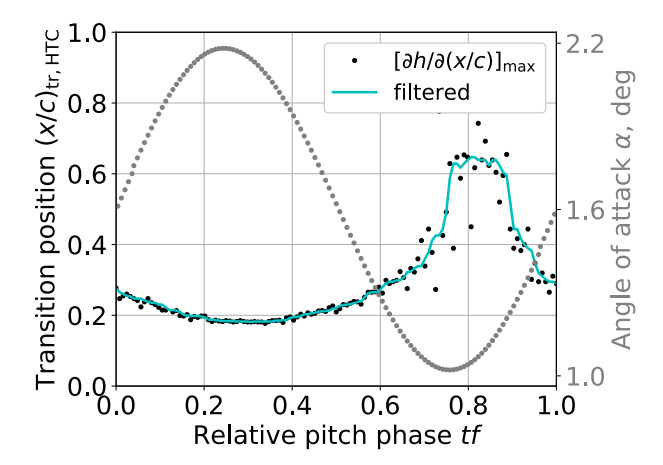


Fig. 14. Transition position results using the HTC method with k=0.108 and $\alpha=1.6\pm0.6$ deg. Black dots: detected maxima of h values; cyan line: smoothed fit using running median filter. Superimposed is the pitch cycle (dotted line).

- 3. Span-wise averaging of ratio images to create line profiles in flow direction
- 4. Conversion of image ratio profiles to temperature differences according to Eq. (9)
- 5. Processing of heat-transfer coefficient (h) profiles using Eqs. (5)–(8) and application of running median filter to these with $\Delta x/c=0.05$
- 6. Detection of maximum gradient $\partial h/\partial(x/c)$ for all phases tf and application of running median filter with $\Delta tf=0.08$

3.2.3. Cycle-to-cycle pressure variations (σc_p)

As a comparison to the results obtained by the DT and HTC methods, unsteady transition locations were additionally derived by means of the σc_p -method according to Gardner and Richter [6]. If the boundarylayer transition position moves across a discrete sensor location, the technique effectively yields the phase positions, where the cycle-tocycle standard deviation of the associated pressure readings reaches a relative maximum. For instance, in Fig. 15, the standard deviation of pressure readings is plotted against the relative pitch phase for a sensor at x/c = 0.17. The graph corresponds to the case where f = 8 Hz(k =0.108) and $\alpha = 1.6 \pm 0.6$ deg. Each dot in the graph corresponds to the standard deviation of samples from 160 pitch cycles. The detected maxima in Fig. 15 are shown by the red filled circles. The first peak indicates boundary-layer transition at $(x/c)_{tr} = 0.17$ at tf = 0.07 during upstroke and at tf = 0.51 during downstroke movement of the airfoil. The obtained results from all pressure transducers for that case are presented in Fig. 16, where the transition locations found for the sensor at x/c = 0.17 are again highlighted in red.

Not all pressure transducer readings yield distinct maxima in the corresponding standard deviation plots. These are the cases if the flow over the pressure transducers is naturally laminar or turbulent during the entire pitch cycle, or if the pressure tap locations are covered by turbulent wedges which originate from disturbances further upstream. However, the σc_n results in Fig. 16 show a downstream movement of boundary-layer transition location in the region 0.5 < tf < 0.8 and an upstream movement for tf > 0.8 and tf < 0.1. For the most part, the upstream and downstream movement of transition locations takes place during upstroke and downstroke of the pitch cycle, which are rendered by open and closed circles, respectively. However, the transducer at $(x/c)_{tr} = 0.31$ indicates downstream movement of boundary-layer transition at tf = 0.79, as the upstroke has already started. This phase shift of boundary-layer transition movement with respect to the pitch cycle is due to the lift-based hysteresis according to Theodorsen [36] and detailed below.

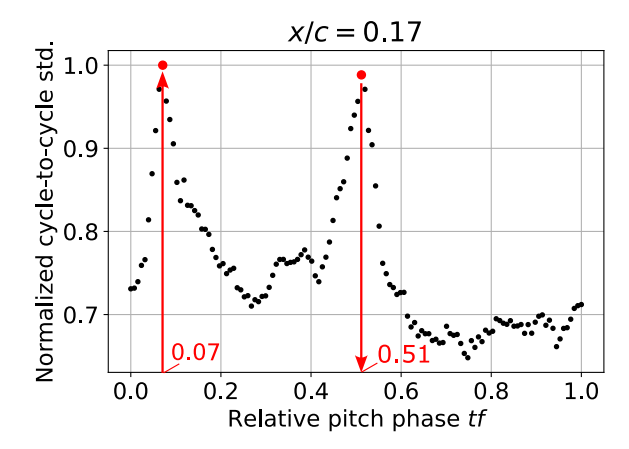


Fig. 15. Standard deviation from 160 pitch cycles of pressure signal σc_p at x/c = 0.17 against relative pitch phase tf for the case at k = 0.108; $\alpha = 1.6 \pm 0.6$ deg. Arrows indicate relative pitch phases when boundary-layer transition moved across $(x/c)_{\rm tr} = 0.17$ during up- (\uparrow) and downstroke (\downarrow) .

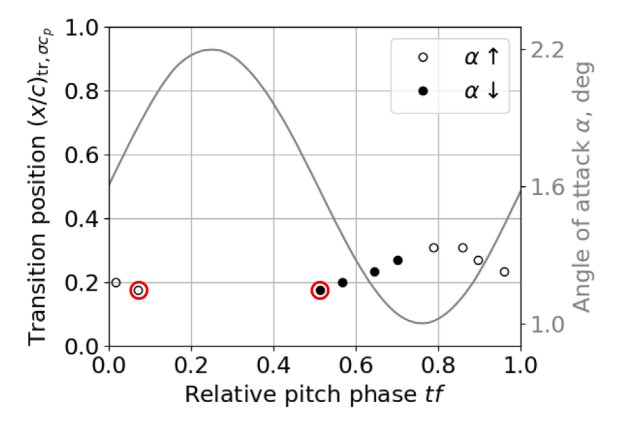


Fig. 16. Transition position results using the σc_p method with k=0.108 and $\alpha=1.6\pm0.6$ deg. Superimposed is the pitch cycle (gray line).

3.2.4. Hysteresis effects

On pitching airfoils, there are different hysteresis effects leading to a time-lag of the boundary-layer transition motion with respect to the pitch angle. In principle, the actual *aerodynamic* hysteresis should be distinguished from the *thermal* hysteresis component when using thermal detection methods:

Aerodynamic hysteresis. The aerodynamic hysteresis can be attributed to both in-viscid and viscous effects. For harmonically pitching airfoils, Theodorsen [36] describes a hysteresis in the lift force with respect to pitch angle. This means that the same instantaneous angle-of-attack leads to different lift forces during up- and downstrokes. The observable time lag between lift and pitching motion is therefore caused by changes in the in-viscid external flow conditions during pitch oscillation. The alternating shed vorticity into the wake and the associated change of circulation cause different induced velocities with direct impact on the pressure distribution and the resulting lift force. In terms of boundary-layer transition, aerodynamic hysteresis means that the transition position passes a certain chord-wise location $(x/c)_{\rm tr}$ at larger instantaneous angles-of-attack (and associated lift coefficients) during upstroke (α \uparrow) than during downstroke (α \downarrow). Hence, a measure for hysteresis is the pitch angle difference between up- and downstroke for a certain transition location, i.e. $\Delta \alpha = \alpha \uparrow -\alpha \downarrow$. However, not all observed boundary-layer transition phenomena on pitch-oscillating airfoils can be explained by Theodorsen's theory. Richter et al. [20] measured the same extent and position of boundary-layer transition during up- and downstroke, but in connection with different pressure distributions (and hence sectional lift). The finding was confirmed by Gardner et al. [37] who also showed that different transition positions occur in connection with similar lift coefficients which were actually based on different pressure distributions. They concluded that the history of the *viscous* boundary-layer profiles needs to be taken into account for a comprehensive modeling of the observed unsteady transition phenomena.

Thermal hysteresis. In addition to the aforementioned aerodynamic component, a thermal hysteresis is introduced as a measurement error when the detection technique relies on surface temperature information. The effect was previously observed and studied in view of the DT method when validated against results from pressure transducers (σc_n) or hot-film recordings [see e.g.16,17,20,38]. This measurementbased artefact originates from the finite thermal response time of a heated model surface temperature with respect to an upstream moving turbulent boundary-layer, for instance, which more effectively cools the surface during the upstroke. In principle, the thermal response can be optimized by an appropriate selection of the model surface material. For instance, a low thermal conductivity λ_s and a low heat capacity per unit volume $\rho_s c_s$ are desirable to achieve both fast response times and large ΔT -signals. However, Gardner et al. [16] showed that the effect of using different surface materials is rather minimal. The relative phase difference $\Delta t f$ between the images considered for the evaluated ΔT signal is the key parameter influencing the thermal hysteresis [16,17]. The best practical recommendation of both studies was to choose $\Delta t f$ as small as possible in order to minimize the thermal hysteresis, while at the same time keeping it as large as possible to deliver a sufficient ΔT signal in order to be able to find significant peaks.

The TSP results in this work are therefore expected to comprise a thermal hysteresis component due to its principle which is based on detecting thermal changes on the model surface as a result of the moving location of boundary-layer transition during pitch-oscillation. However, the TSP sensor used in this work, Ru(terpy)₂Cl₂, should in principal be capable to follow a transition movement for oscillations of up to 40 Hz (see Table 1). For the same sensor, Klein et al. [39] showed under cryogenic conditions that periodic events of at least 100 Hz could be detected and that the response time is in the order of only a few milliseconds.

A scaling parameter for hysteresis of transition positions on harmonically pitching airfoils was found by Wolf et al. [17]. They showed that the measured hysteresis effectively scales with the pitch rate $\partial \alpha/\partial t$, at least for a specific transition location. For a sinusoidal pitching motion, the pitch rate is proportional to both, pitch frequency f and pitch amplitude $\hat{\alpha}$ (see Eq. (10)).

$$\frac{\partial \alpha}{\partial t} = 2\pi \hat{\alpha} f \cos(2\pi t f) \tag{10}$$

Assuming that the σc_p method captures the effect of aerodynamic hysteresis without additional thermal lag, the additional measurement-based thermal hysteresis can be isolated by subtracting the component measured by means of the σc_p technique from the hysteresis measured using thermal techniques (see also [17,38]).

4. Results comparison and technique evaluation

The unsteady transition positions obtained from the three above detailed methods are plotted against the relative pitch phase and compared for the pitching motion at k=0.108; $\alpha=1.6\pm0.6$ deg in Fig. 17. As a reference, and in order to facilitate interpretation of results, the steady result obtained from the fitted curve to the experimental data (see Fig. 6) has also been plotted, along with a plot of the angle-of-attack of the pitching motion. Error bars were estimated and are shown at two representative phase positions. The error in phase is based on the temporal resolution of the data and always lies within the symbol size of the respective method. The size of the error bars of the σc_p method is derived from the spatial resolution of the sensors upstream

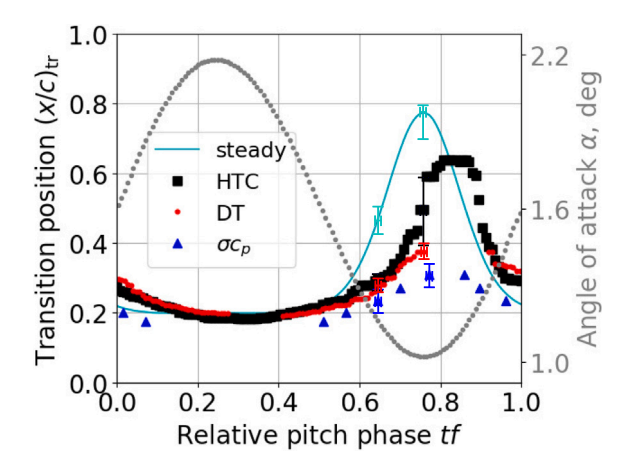


Fig. 17. Transition locations as a function of pitch phase at k=0.108; $\alpha=1.6\pm0.6$ deg for the three different transition detection techniques, including a comparison with the steady results.

and downstream of the indicated location. The error bars of the DT and HTC results correspond to the random scatter of the results in the range of $\Delta t f = \pm 0.016$ with respect to the indicated phase, while those of the steady polar have been estimated from the respective deviation of sampled steady data points and the exponential fit shown in Fig. 6.

The upstream and downstream motion of boundary-layer transition during upstroke and downstroke has been captured by all detection methods and a phase shift of the detected transition motion is inherent to all unsteady results when compared to the steady data. The σc_n results yield transition locations further upstream compared to the results of the thermal techniques. The difference to the HTC results is smaller at tf < 0.7 (with $\Delta(x/c)_{tr} \approx 0.04$) and larger at tf > 0.75where $\Delta(x/c)_{tr}$ < 0.3. Possible reasons for the systematic deviations are span-wise inhomogeneities of inflow conditions and model geometry, i.e. deviations from truly 2D conditions. The pressure transducers were placed in the center of the model in contrast to the cntTSP coating, whose upper boundary was placed two chord lengths closer to the wind tunnel floor (see Fig. 3). Moreover, it is also possible that the pressure tappings introduce disturbances to the boundarylayer flow which cause premature boundary-layer transition. In the range 0.1 < tf < 0.5, no σc_p results are available. During this phase period, the results obtained by the HTC method suggest that boundarylayer transition moves about $\Delta(x/c)_{\rm tr} \approx 0.04$ up- and downstream. However, the phase averaged recordings of the two pressure sensors just upstream of $(x/c)_{tr} = 0.17$ that could have captured a similar relative up- and downstream movement for the σc_p results were not able to identify any distinct peaks, probably because the flow over the respective transducers had been turbulent during the entire pitch cycle.

When regarding the results of the HTC method, it is remarkable that this technique yields results over the entire pitch cycle. In contrast, the DT results lack data points during pitch phases just after the pitch reversal from up- to downstroke movement and vice-versa. The DT results rely on a single temperature difference between two images recorded with a certain relative phase difference $\Delta t f$. Close to the pitch reversal points, the DT signal is hampered by thermal hysteresis and comprises a double-peak which makes it impossible to unambiguously identify boundary-layer transition (see Section 3.2.1 and [16,17]). For the HTC method, on the other hand, the transition location at a single phase results from the integration of temperature differences across the entire pitch-cycle and the temperature differences closer to the phase under investigation carry a greater weight (see Eq. (8)). In other words, the HTC signal is a weighted sum of DT signals where the disadvantages of a single DT signal close to the pitch reversal points have been smeared out by summation. Other than close to the pitch reversal points, the HTC and DT results are remarkably similar.

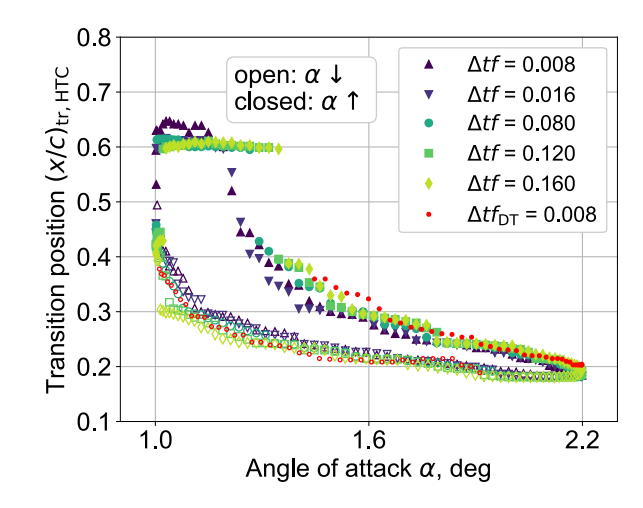


Fig. 18. Transition locations from the HTC method as a function of pitch angle $\alpha=1.6\pm0.6$ deg with k=0.108 for different relative phase differences Δtf .

A more detailed examination of the plot in Fig. 17 shows that DT results possess a phase lag of about $\Delta t f \approx 0.02$ relative to the HTC results. It should be noted that the displayed DT results were derived using a relative phase difference of $\Delta t f = 0.080$ between the images used for the calculation of the individual temperature differences as a basis for the peak detection (see Section 3.2.1). In contrast, the HTC results were processed using a lower value of $\Delta t f = 0.008$ for the calculation of the respective temperature differences used in the summation according to Eq. (8). Although for the DT technique a value of $\Delta t f = 0.008$ principally also yielded results (as outlined further in Section 4.1) the chosen values for $\Delta t f$ were taken because they yielded the best results for the respective methods in terms of minimization of thermal hysteresis while maximizing the amount of detected transition locations across the pitch cycle.

4.1. Influence of relative phase difference between images

The DT and HTC results for the test point discussed in Fig. 17 were evaluated for seven different relative phase differences ranging from $\Delta t f = 0.008 - 0.160$. In Fig. 18, the transition positions detected by the HTC method are plotted against the angle-of-attack for selected image separations. In Fig. 18 and the following figures, open and closed symbols correspond to the downstroke (1) and upstroke (1) motion, respectively. For large image separations, the HTC results show no detected transition locations between $0.3 < (x/c)_{tr} < 0.4$ close to the downstroke/upstroke pitch reversal (for $\Delta t f \ge 0.12$) and also between $0.4 < (x/c)_{\rm tr} < 0.6$ (for $\Delta t f \ge 0.080$) during up- and downstroke in the chord-wise region where transition is particularly sensitive to changes in pitch angle. Wolf et al. [17] showed on a different pitch-oscillating airfoil that for these particular pitch phases (close to the pitch reversal point where boundary-layer transition is sensitive with respect to angleof-attack) the ΔT signals used for the DT method become erroneous if the image separation is too large. Close to pitch reversal, there are the above-mentioned coexisting positive- and negative ΔT peaks and when the transition movement is fast, the ΔT signal spreads and leads to a double peak (see Figs. 17 + 19 in [17]). Since according to Eq. (8) the HTC results include a weighted sum of ΔT signals (which are used individually for the DT method), the same effects as detailed by Wolf et al. [17] explain the erroneous HTC results in the above-mentioned regions. Note that for the HTC method, only the smallest relative phase difference of $\Delta t f = 0.008$ is capable of capturing the fast upstream and downstream movement of boundary-layer transition between 0.45 < $(x/c)_{\rm tr}$ < 0.65 during upstroke and downstroke, respectively, also without a lack of results between $0.3 < (x/c)_{tr} < 0.4$.

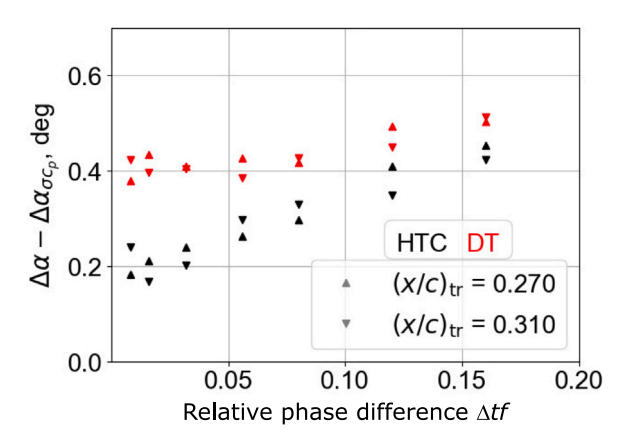


Fig. 19. Thermal hysteresis as a function of relative phase difference at k = 0.108 and for $\alpha = 1.6 \pm 0.6$ deg for two different transition locations.

The hysteresis of HTC results between $0.2 < (x/c)_{tr} < 0.4$ decreases with decreasing relative phase difference $\Delta t f$. The observation confirms the findings for the DT technique by Wolf et al. [17] and is again plausible due to the integrating nature of the HTC profiles with respect to the ΔT signals used for the DT method in Eq. (8). For a comparison with the DT technique, and to simplify the visualization of the plots in Fig. 18, the DT result with only the shortest evaluated relative phase difference $\Delta t f = 0.008$ has been added to the figure (see red dots (•). Whereas the HTC result at $\Delta t f = 0.008$ yielded data for the entire pitch cycle, the DT algorithm could not detect any transition positions downstream of $(x/c)_{tr} > 0.38$ or just upstream of $(x/c)_{tr} < 0.2$. The lack of results for the DT method is due to the above-mentioned inherent difficulties in detecting boundary-layer transition in temporal proximity to the pitch reversal phases. Note that the relative phase difference of $\Delta t f = 0.008$ corresponds to the minimum relative phase difference between two images recorded in direct succession at 1 kHz frame rate and at 8 Hz pitch frequency. Thus, the corresponding DT result is expected to yield the lowest thermal hysteresis for the DT method. It is remarkable however, that the HTC result for $\Delta t f = 0.008$ outperforms the corresponding DT result by showing a significantly lower hysteresis in terms of $\Delta \alpha$ at constant $(x/c)_{tr}$.

At transition positions where σc_p results are available (see Fig. 17, not shown in Fig. 18 for the sake of clarity), the thermal hysteresis was isolated by subtracting the aerodynamic contribution (derived from σc_p) from the hysteresis detected by the thermal methods, i.e. $\Delta \alpha_{\rm thermal} = \Delta \alpha_{\rm HTC|DT} - \Delta \alpha_{\sigma c_p}$ [17]. For the measurement point discussed above, this was done at two positions $((x/c)_{\rm tr} = 0.27$ and 0.31) and the results are plotted in Fig. 19 as a function of the altered relative phase difference.

The graph reveals that the HTC results (black symbols) have a systematically lower thermal hysteresis than the DT results (red symbols), even when compared at the same values for Δtf . The reasoning for this finding had been addressed previously in schematic form in Fig. 7, which displays the ΔT signal peaks systematically too far downstream during upstroke and too far upstream during downstroke when compared to the actual transition position. If it is again taken into account, that for a distinct phase, the heat-transfer coefficient for the HTC method considers a sum of ΔT signals of the entire pitch cycle, it appears that upstream and downstream differences to the actual transition position partly cancel out such that the integrated difference to the actual transition position eventually decreases. The cancellation is limited because according to Eq. (8), the weighting of all ΔT signals in the pitch cycle is stronger the shorter the respective phase difference with respect to the phase under consideration.

In addition to the systematic difference between the DT and HTC methods, as shown in Fig. 19, both detection techniques showed decreased thermal hysteresis at lower values for $\Delta t f$. However, this effect

disappears at $\Delta t f \leq 0.080$ for the DT method and at $\Delta t f \leq 0.032$ for the HTC method. At these image separations, an additional decrease of $\Delta t f$ does not lead to a further decrease of the thermal hysteresis component, as had been numerically predicted to diminish when the relative phase difference approaches zero [16]. For experimental (image) data however, this saturation effect had also been observed by Wolf et al. [17], who attributed it to random scatter affecting the signalto-noise ratio of calculated temperature differences when using the short image separations. Gardner et al. [16] demonstrated that close to pitch reversal, where surface temperature differences due to boundarylayer transition movement from the downstroke movement have been superimposed onto temperature differences from the upstroke movement, the ΔT signals become less ambiguous with decreasing $\Delta t f$. For the HTC method it should therefore be noted that results with the lowest possible relative phase difference should be adopted. In this manner, even for pitch phases not close to the pitch reversal, the influence of ambiguous ΔT signals from close to the pitch reversal points will be decreased when they have been summed, as in the HTC post-processing using Eq. (8).

To conclude, the optimal relative phase difference between processed images for the DT method is $\Delta tf=0.080$. It leads to the minimum achievable thermal hysteresis (at $(x/c)_{\rm tr}=0.27$ and $(x/c)_{\rm tr}=0.31$) and yet has larger ΔT signal-to-noise ratios as with the smaller values of Δtf ; this is not shown here but had also been observed by Wolf et al. [17]. In analogy, the optimal relative phase difference for the HTC method with respect to lowest possible thermal hysteresis would be at $\Delta tf=0.032$. However, as indicated in the results shown in Fig. 18 and as discussed above, the HTC method should be the one of choice with its lowest possible image separation, so that fast gradients of the boundary-layer transition movement can best be resolved. It should also be noted that the found optima for Δtf are not universal but depend on the experimental setup. The lower limit is mainly governed by the signal-to-noise ratio of the employed camera and the temperature sensitivity of the TSP.

In the following studies, the HTC data have been processed using $\Delta t f = 0.04$. This parameter value was chosen such that all displayed data points could be processed with the same $\Delta t f$. In this way, the effects of reduced pitch frequency and pitch amplitude could be isolated. The pitch frequency was increased to k = 0.540, where a relative phase difference of $\Delta t f = 0.04$ corresponds to the relative phase difference between two successively acquired images.

4.2. Influence of pitch frequency

In Fig. 20, the HTC transition positions for the case $\alpha=1.2\pm0.2$ deg have been plotted against angle-of-attack for reduced frequencies of k=0.108,0.270 and 0.540. For all reduced frequencies, the transition motion was detected in the range $0.27 < (x/c)_{\rm tr} < 0.65$. As expected from Theodorsen's theory, the hysteresis $\Delta\alpha$ increases with increasing k.

The HTC results show a noticeable step between $0.4 < (x/c)_{\rm tr} < 0.65$, where also for the previously discussed results (e.g. in Fig. 18) difficulties had been identified in resolving the transition movement in the particularly pitch-angle sensitive regions; this is as shown by the steady polar in Fig. 6. It should be mentioned here, that the HTC results for this case could not be improved by using the smallest possible relative phase difference of $\Delta tf = 0.008$, as it had been successfully applied for the case presented in Fig. 18 where a larger pitch amplitude at the same reduced frequency had applied. Weiss et al. [38] showed that the ΔT signal due to moving boundary-layer transition is reduced for decreasing pitch amplitudes at constant pitch frequency. Hence, the reduction of the pitch amplitude from $\hat{\alpha} = 0.6$ (see Fig. 18) to $\hat{\alpha} = 0.2$ (see Fig. 20) presents a limit to the application of the HTC method in terms of its capability to resolve the fast transition movement between $0.45 < (x/c)_{\rm tr} < 0.62$.

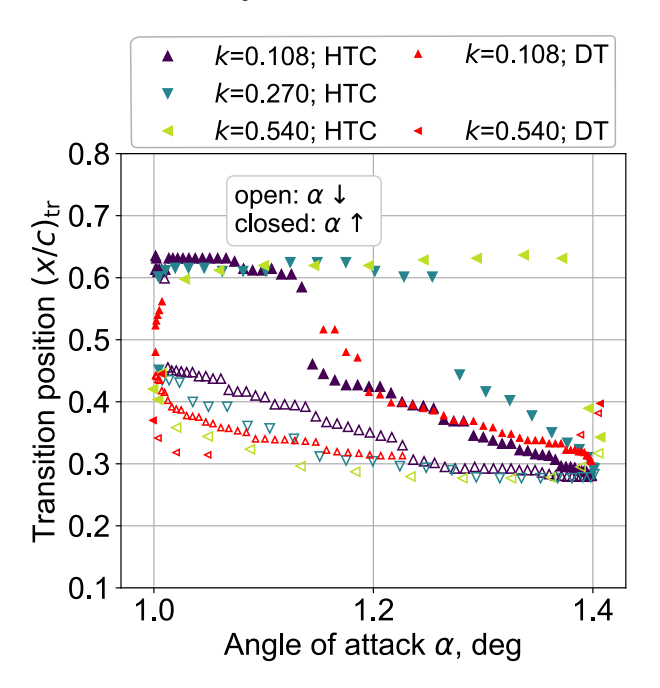


Fig. 20. Transition positions from the HTC and DT methods as a function of pitch angle α at $\alpha=1.2\pm0.2$ deg and for different pitch frequencies k=0.108,0.270 and 0.540.

For the cases with the smallest and largest reduced frequencies, the DT results have been added to the plot in Fig. 20 using the same symbols as for the HTC method, only in red color. At k=0.540 the DT method could hardly detect any transition positions which would describe a coherent transition motion. This was due to the poor signal quality of the respective ΔT profiles with their either negligible peak prominence or their ambiguous double peaks. A deterioration in ΔT -signal quality at large pitch frequencies had been measured previously by Weiss et al. [38]. They attributed the effect to the reduced time (at larger frequencies) for the model surface to react to the changing boundary-condition of the heated model surface between the two time instants of the processed images for the chosen relative phase difference. At k=0.108 the DT results show again a greater hysteresis than those provided by the HTC method, especially between $0.3 < (x/c)_{\rm tr} < 0.45$.

Unfortunately, the pressure transducer recordings for the above mentioned cases did not provide sufficient results to show any trends with alternating reduced pitch frequencies. A more detailed comparison between the findings of the thermal methods and the σc_p technique is provided in the next section.

4.3. Influence of pitch amplitude

The results of the pitch amplitude study are plotted in Fig. 21 for the case at $\overline{a}=1.6$ deg, k=0.108 and with pitch amplitudes $\hat{a}=0.2,0.4$ and 0.6. For clarity, the results as obtained by the different techniques DT, HTC and σc_p are shown in separate upper, middle and lower graphs, respectively. Similar to the results in Fig. 17, the σc_p results are seen to lie systematically further upstream than with the thermal methods; this is most likely due to disturbances introduced by the pressure taps themselves, to deviations from truly 2D boundary-conditions for the inflow and from the model geometry and structure. The number of result points is again largest for the HTC method, which is capable of detecting transition positions close the pitch angle reversal points. On the contrary, the DT results are consistently lacking at those periods of the pitch cycle where the most up- and downstream transition positions are to be expected.

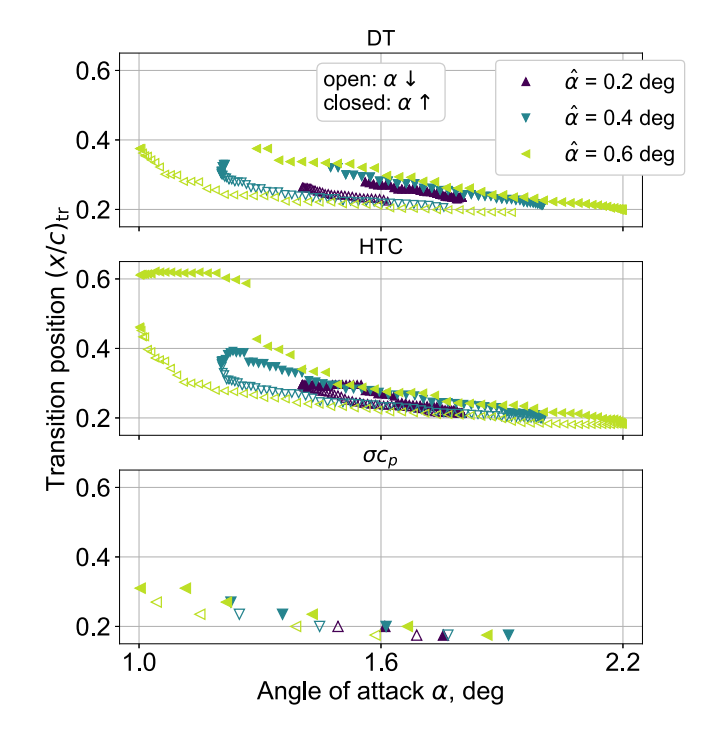


Fig. 21. Transition positions obtained from DT (top), HTC (middle) and σc_p (bottom) methods as a function of angle-of-attack at $\bar{\alpha}=1.6$ deg and k=0.108 for different pitch amplitudes $\hat{\alpha}$.

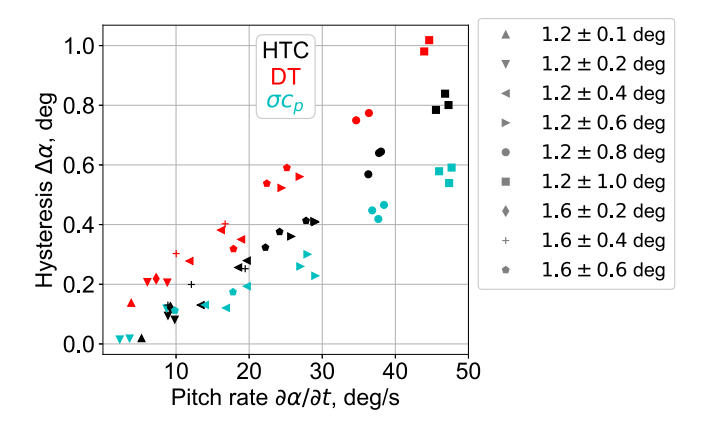


Fig. 22. Transition hysteresis as a function of pitch rate for all three detection methods. Hysteresis is evaluated at $(x/c)_{\rm tr}=0.27,0.31$ and 0.35 for different test cases at k=0.108.

At increasing pitch amplitudes, all methods yield an increased boundary-layer transition region $\Delta(x/c)_{tr}$ as well as increased hysteresis. This hysteresis was further evaluated at transition positions, where all three detection methods have results, i.e. at $(x/c)_{tr} = 0.27, 0.31$ and 0.35. This was done for all the test cases mentioned under "pitch amplitude" study in Table 1. For each test case and each of the mentioned transition positions, the hysteresis value $\Delta \alpha$ is plotted against the respective pitch rate $\partial \alpha / \partial t$ in Fig. 22. The pitch rate associated with each data point is determined as the mean value between the two phases when boundary-layer transition passes the same stream-wise transition position. For each of the detection methods, the processed hysteresis curves increase steadily but with different slopes at increasing pitch rates. This behavior had been previously hypothesized and measured by Wolf et al. [17] on a different 2D-pitching airfoil and had been measured by Weiss et al. [38] on a rotating blade under cyclic pitch conditions. The results shown in Fig. 22 show different trend curves for the three detection methods. The DT results show systematically larger

hysteresis than the HTC results, but both these thermal techniques have larger hysteresis compared to the σc_p data, which latter measures only the aerodynamic hysteresis while not being influenced by any thermally induced lag. When considering the hysteresis difference of the two thermal methods (DT and HTC) compared with the σc_p method results as a measure of the thermal hysteresis (as for Fig. 19), the obtained trends indicate that the HTC method has approximately half the thermal lag compared to the DT method. For instance, at $\partial \alpha/\partial t \approx 45~{\rm deg/s}$, the thermal hysteresis added by the HTC method is only $\Delta \alpha_{\rm thermal,HTC} = \Delta \alpha_{\rm HTC} - \Delta \alpha_{\sigma c_p} \approx 0.2~{\rm deg}$ as opposed to $\Delta \alpha_{\rm thermal,DT} \approx 0.4~{\rm deg}$ for the DT method.

5. Conclusions

This paper presents the first study of unsteady boundary-layer transition on a harmonically pitching airfoil under cryogenic conditions. Boundary-layer transition was detected on a moving 2D airfoil at Re = 6×10^6 using previously established methods based on the variation of unsteady pressure transducer data (σc_p) and differential thermography (DT) using TSP. Whereas the former method allows the detection at discrete chordwise positions only, DT yields data at high spatial resolution, yet with a lack of results at pitch angles close to the minimum and maximum of the pitch cycle. In addition, a detection algorithm based on the qualitative distribution of the heat transfer coefficient (HTC) is presented and validated against σc_p and DT. The main conclusions are summarized as follows:

- Boundary-layer transition could be successfully measured using all three methods. The measurement results obtained on the oscillating airfoil compare well to the results obtained on the steady airfoil showing a phase lag for the unsteady data which is mainly due to aerodynamic hysteresis and for the thermal methods also partly due to measurement related effects.
- The DT technique allows omitting reference images which are usually necessary when detecting boundary-layer transition with TSP on steady airfoils.
- The effects of varying pitch frequency and pitch amplitude on the movement of boundary-layer transition have been successfully determined, whereby similar results were obtained for the three methods.
- 4. The HTC algorithm yields results with high spatial resolution and across the entire pitch cycle, therefore overcoming the drawbacks of the σc_n and DT methods.
- 5. The evaluated transition hysteresis scales with the applicable pitch rate for all three methods. The hysteresis measured using the HTC algorithm is smaller than that using DT, yet is still larger than just the aerodynamic hysteresis, as measured using σc_p method.
- 6. Lower relative phase differences of the images used for the processing of HTC results yield lower thermal, measurementbased, hysteresis. Compared to the DT method, the minimal achievable thermal hysteresis could be halved using the HTC algorithm.

CRediT authorship contribution statement

Armin Weiss: Writing – review & editing, Writing – original draft, Visualization, Validation, Software, Project administration, Methodology, Investigation, Funding acquisition, Formal analysis, Data curation, Conceptualization. Christian Klein: Writing – review & editing, Supervision, Resources, Project administration, Methodology, Investigation, Funding acquisition, Data curation. Ulrich Henne: Writing – review & editing, Software, Investigation, Formal analysis, Data curation. Anne Hebler: Investigation, Data curation.

Declaration of competing interest

The authors declare that they have no known competing financial interests or personal relationships that could have appeared to influence the work reported in this paper.

Acknowledgments

The authors would like to thank Vladimir Ondrus (University of Applied Sciences Münster) for the synthesis of the ruthenium complex used in this work. We also appreciate the help of Carsten Fuchs and Tobias Kleindienst (both DLR Göttingen) for setting up the TSP experiment, and especially for polishing the model to the desired TSP surface roughness. The authors further thank the colleagues from DNW in Göttingen, Martin Bruse and Heiko Uhlemann, as well as the colleagues from DNW in Cologne (which are now with DLR), Junnai Zhai, Edgar Augenstein, Frank Narres, Thomas Meyer, Amand Vree and Sebastian Melzer, for their support during the campaign and for operating the facility. Thank you also to our DLR colleagues from the institute of aeroelastics, Holger Mai, Johannes Nuhn, Heiko Böhlken, Thomas Büte and Janis Lübker for model and test rig integration into the wind tunnel.

Data availability

The authors will share result figures of this work upon request.

References

- IATA, Net-Zero Carbon Emissions by 2050, International Air Transport Association (IATA), 2021, https://www.iata.org/en/pressroom/pressroom-archive/2021-releases/2021-10-04-03/. (Accessed 15 August 2024).
- [2] A. Seitz, A. Hübner, K. Risse, The DLR TuLam project: Design of a short and medium range transport aircraft with forward swept NLF wing, CEAS Aeronaut. J. 11 (2) (2020) 449–459, URL: https://doi.org/10.1007/s13272-019-00421-1.
- [3] H. Mai, A. Hebler, S. Koch, High Reynolds number testing of a laminar airfoil under forced harmonic pitching oscillations at cryogenic conditions, in: International Forum on Aeroelasticity and Structural Dynamics, IFASD 2019, Savannah, Georgia, USA, 2019, pp. 1–14, IFASD-2019-112. URL: https://elib. dlr.de/127974/1/IFASD-2019-112.pdf.
- [4] M. Braune, H. Mai, A. Hebler, Influence of laminarity on the aeroelastic behavior of the NLR7301 airfoil, in: International Forum on Aeroelasticity and Structural Dynamics, IFASD 2022, Madrid, Spain, 2022, pp. 1–19, IFASD-2022-126. URL: https://elib.dlr.de/187136/1/Braune Mai Hebler 2022.pdf.
- [5] P.F. Lorber, F.O. Carta, Unsteady transition measurements on a pitching three-dimensional wing, in: 5th Symposium on Numerical and Physical Aspects of Aerodynamic Flows, Long Beach, CA, USA, 1992, pp. 1–14, URL: https://ntrs.nasa.gov/api/citations/19930018261/downloads/19930018261.pdf.
- [6] A.D. Gardner, K. Richter, Boundary layer transition determination for periodic and static flows using phase-averaged pressure data, Exp. Fluids 56 (6) (2015) 119–131, URL: https://10.1007/s00348-015-1992-9.
- [7] A.P. Colburn, A method of correlating forced convection heat transfer data and a comparison with fluid friction, Trans. Am. Inst. Chem. Eng. 29 (1933) 174–206, URL: https://doi.org/10.1016/0017-9310(64)90125-5.
- [8] T. Chilton, A. Colburn, Mass transfer (absorption) coefficients prediction from data on heat transfer and fluid friction, Ind. Eng. Chem. 26 (1934) 1183–1187, URL: https://pubs.acs.org/doi/epdf/10.1021/ie50299a012.
- [9] A.V. Popov, R.M. Botez, M. Labib, Transition point detection from the surface pressure distribution for controller design, J. Aircr. 45 (1) (2008) 23–28, URL: https://doi.org/10.2514/1.31488.
- [10] T. Liu, J.P. Sullivan, K. Asai, C. Klein, Y. Egami, Pressure and Temperature Sensitive Paints, second ed., in: Experimental Fluid Mechanics, Springer Cham, 2021, URL: https://doi.org/10.1007/978-3-030-68056-5.
- [11] H. Schlichting, K. Gersten, Boundary-Layer Theory, nineth ed., Springer-Verlag Berlin Heidelberg, 2017, URL: https://doi.org/10.1007/978-3-662-52919-5.
- [12] U. Fey, R.H. Engler, Y. Egami, Y. Iijima, K. Asai, U. Jansen, J. Quest, Transition detection by temperature sensitive paint at cryogenic temperatures in the European transonic windtunnel (ETW), in: 20th International Congress on Instrumentation in Aerospace Simulation Facilities, IEEE, 2003, pp. 77–88, http://dx.doi.org/10.1109/ICIASF.2003.1274855, URL: https://ieeexplore.ieee.org/stamp/stamp.jsp?tp=&arnumber=1274855.

- [13] C. Klein, U. Henne, W. Sachs, U. Beifuss, V. Ondrus, M. Bruse, R. Lesjak, M. Löhr, Application of carbon nanotubes (CNT) and temperature-sensitive paint (TSP) for the detection of boundary layer transition, in: 52nd Aerospace Sciences Meeting, National Harbor, MD, USA, 2014, pp. 1–8, AIAA 2014-1482. URL: https://arc.aiaa.org/doi/abs/10.2514/6.2014-1482.
- [14] C. Klein, U. Henne, Y. Deisuke, V. Ondruss, U. Beifuss, A.-K. Hensch, J. Quest, Application of carbon nanotubes and temperature sensitive paint for the detection of boundary layer transition under cryogenic conditions (invited), in: 55th AIAA Aerospace Sciences Meeting, Grapevine, TX, USA, 2017, pp. 1–10, http://dx.doi.org/10.2514/6.2017-0336, AIAA 2017-0336. URL: https://arc.aiaa.org/doi/abs/10.2514/6.2017-0336.
- [15] U. Fey, Y. Egami, Transition detection by temperature-sensitive paint, in: C. Tropea, A. Yarin, J.F. Foss (Eds.), Springer Handbook of Experimental Fluid Mechanics, Springer-Verlag Berlin Heidelberg, 2007, pp. 537–552, http://dx.doi.org/10.1007/978-3-540-30299-5 7.
- [16] A.D. Gardner, C. Eder, C.C. Wolf, M. Raffel, Analysis of differential infrared thermography for boundary layer transition detection, Exp. Fluids 58 (9) (2017) 122, URL: https://doi.org/10.1007/s00348-017-2405-z.
- [17] C.C. Wolf, C. Mertens, A.D. Gardner, C. Dollinger, A. Fischer, Optimization of differential infrared thermography for unsteady boundary layer transition measurement, Exp. Fluids 60 (19) (2019) 1–13, URL: https://doi.org/10.1007/ s00348-018-2667-0.
- [18] C.C. Wolf, Differential Infrared Thermography for Rotor Aerodynamics (Ph.D. thesis), Gottfried Wilhelm Leibniz Universität Hannover, 2023, p. 158, URL: https://doi.org/10.15488/14143.
- [19] M. Raffel, C.B. Merz, Differential infrared thermography for unsteady boundary-layer transition measurements, AIAA J. 52 (9) (2014) 2090–2093, URL: https://doi.org/10.2514/1.J053235.
- [20] K. Richter, C.C. Wolf, A.D. Gardner, C.B. Merz, Detection of unsteady boundary layer transition using three experimental methods, in: 54th AIAA Aerospace Sciences Meeting, San Diego, CA, USA, 2016, pp. 1–22, AIAA 2016-1072. URL: https://doi.org/10.2514/6.2016-1072.
- [21] D. Yorita, J. Lemarechal, C. Klein, K. Fujita, H. Nagai, Transition detection methods in a pitch-sweep test by means of TSP using lifetime and intensity measurements, in: AIAA Scitech 2020 Forum, American Institute of Aeronautics and Astronautics, Orlando, FL, USA, 2020-01-06, pp. 1–9, AIAA 2020-0296. URL: https://doi.org/10.2514/6.2020-0296.
- [22] T. Ikami, K. Fujita, H. Nagai, D. Yorita, Measurement of boundary layer transition on oscillating airfoil using cntTSP in low-speed wind tunnel, Meas. Sci. Technol. 32 (7) (2021) 075301, URL: http://dx.doi.org/10.1088/1361-6501/abe2be.
- [23] J. Zhai, Statement on peniche thickness for half-model testing in DNW's cryogenic wind tunnel in Cologne, 2024, private communication.
- [24] C. Klein, A. Weiss, U. Henne, Application of temperature sensitive paint for time resolved investigations of laminar-to-turbulent transition on oscillating airfoils, in: AIAA Scitech 2022 Forum, San Diego, CA & Virtual, USA, 2022, pp. 1–12, AIAA 2022-1717. URL: https://doi.org/10.2514/6.2022-1717.
- [25] C. Klein, U. Henne, M. Costantini, V. Ondrus, U. Beifuss, J. Zhai, J. Quest, Development of a highly sensitive temperature-sensitive paint for measurements under cryogenic temperature (100 - 160 K) conditions, in: 54th AIAA Aerospace Sciences Meeting, San Diego, CA, USA, 2016-01-04, pp. 1–9, AIAA 2016-0650. URL: https://doi.org/10.2514/6.2016-0650.
- [26] C. Klein, R.H. Engler, U. Henne, W.E. Sachs, Application of pressure-sensitive paint for determination of the pressure field and calculation of the forces and moments of models in a wind tunnel, Exp. Fluids 39 (2) (2005) 475–483, http:// dx.doi.org/10.1007/s00348-005-1010-8, URL: https://doi.org/10.1007/s00348-005-1010-8.
- [27] M. Costantini, U. Henne, S. Risius, C. Klein, A robust method for reliable transition detection in temperature-sensitive paint data, Aerosp. Sci. Technol. 113 (2021) 106702, http://dx.doi.org/10.1016/j.ast.2021.106702, URL: https://www.sciencedirect.com/science/article/pii/S1270963821002121.
- [28] M. Drela, M.B. Giles, Viscous-inviscid analysis of transonic and low Reynolds number airfoils, in: AIAA Journal, AIAA J. 25 (10) (1987) 1347–1355, URL: https://doi.org/10.2514/3.9789.
- [29] M. Drela, Newton solution of coupled viscous/inviscid multielement airfoil flows, in: 21st Fluid Dynamics, Plasma Dynamics and Lasers Conference, Seattle, WA, USA, 1990, pp. 1–10, URL: https://doi.org/10.2514/6.1990-1470.
- [30] W.J. Cook, E.J. Felderman, Reduction of data from thin-film heat-transfer gages: A concise numerical technique, AIAA J. 4 (3) (1966) 561–562, URL: https://doi.org/10.2514/3.3486.
- [31] W.J. Cook, Determination of heat-transfer rates from transient surface temperature measurements, AIAA J. 8 (7) (1970) 1366–1368, URL: https://doi.org/10. 2514/3.5909.
- [32] R.J. Vidal, C.E. Wittliff, C.E. Bartlett, J.G. Logan, Investigation of Stagnation Point Heat Transfer in the C.A.L. Hypersonic Shock Tunnel, Technical report AA-966-A-1, Cornell Aeronautical Laboratory, 1955.
- [33] J.J. Jones, Shock-Tube Heat-Transfer Measurements on Inner Surface of a Cylinder (Simulating a Flat Plate) for Stagnation-Temperature Range 4,100° to 8,300°R, Technical Report NASA TN D-54, NASA, 1962.

- [34] S. Risius, W.H. Beck, C. Klein, U. Henne, A. Wagner, Determination of heat transfer into a wedge model in a hypersonic flow using temperature-sensitive paint, Exp. Fluids 58 (9) (2017) 117, URL: https://doi.org/10.1007/s00348-017-2393-z.
- [35] C. Mertens, C.C. Wolf, A.D. Gardner, F.F.J. Schrijer, B.W. van Oudheusden, Advanced infrared thermography data analysis for unsteady boundary layer transition detection, Meas. Sci. Technol. 31 (1) (2019) 015301, URL: http: //dx.doi.org/10.1088/1361-6501/ab3ae2.
- [36] T. Theodorsen, General theory of aerodynamic instability and the mechanism of flutter, Technical Report 496, NACA, 1935, URL: https://ntrs.nasa.gov/api/ citations/19930090935/downloads/19930090935.pdf.
- [37] A.D. Gardner, C.B. Merz, C.C. Wolf, Effect of sweep on a pitching finite wing, J. Am. Helicopter Soc. 64 (3) (2019) 1–13, http://dx.doi.org/10.4050/JAHS.64.032007, URL: https://www.ingentaconnect.com/content/ahs/jahs/2019/00000064/00000003/art00007.
- [38] A. Weiss, C.C. Wolf, K. Kaufmann, J.N. Braukmann, J.T. Heineck, M. Raffel, Unsteady boundary-layer transition measurements and computations on a rotating blade under cyclic pitch conditions, Exp. Fluids 61 (2) (2020) 61, URL: https://doi.org/10.1007/s00348-020-2899-7.
- [39] C. Klein, S. Risius, U. Henne, V. Ondrus, Determination of the response time of TSP in cryogenic conditions, in: AIAA Scitech 2024 Forum, Orlando, FL, USA, 2024, pp. 1–12, AIAA 2024-1093. URL: https://doi.org/10.2514/6.2024-1093.